

Key Points:

- Monthly time series of carbonate variables were reconstructed from 1982 to 2015 for the Mid-Atlantic Bight and the South Atlantic Bight
- The rate of fugacity of CO₂ increase in the Mid-Atlantic Bight was faster than those in the South Atlantic Bight and the open ocean
- Seasonal asymmetry in the evolution of long-term change of aragonite saturation state leads to an increase in seasonal amplitude

Supporting Information:

- Supporting Information S1
- Figure S1
- Figure S2
- Figure S3
- Figure S4
- Figure S5
- Figure S6
- Figure S7
- Figure S8
- Figure S9
- Figure S10

Correspondence to:

W.-J. Cai,
wcai@udel.edu

Citation:

Xu, Y.-Y., Cai, W.-J., Wanninkhof, R., Salisbury, J., Reimer, J., & Chen, B. (2020). Long-Term Changes of Carbonate Chemistry Variables Along the North American East Coast. *Journal of Geophysical Research: Oceans*, 125, e2019JC015982. <https://doi.org/10.1029/2019JC015982>

Received 16 DEC 2019

Accepted 19 MAY 2020

Accepted article online 5 JUN 2020

Long-Term Changes of Carbonate Chemistry Variables Along the North American East Coast

Yuan-Yuan Xu^{1,2,3} , Wei-Jun Cai¹ , Rik Wanninkhof³ , Joseph Salisbury⁴ , Janet Reimer¹, and Baoshan Chen¹ 

¹School of Marine Science and Policy, University of Delaware, Newark, DE, USA, ²Now at Cooperative Institute for Marine and Atmospheric Studies, University of Miami, Miami, FL, USA, ³NOAA Atlantic Oceanographic and Meteorological Laboratory, Miami, FL, USA, ⁴Ocean Processes Analysis Laboratory, University of New Hampshire, Durham, NH, USA

Abstract Decadal variability of carbonate chemistry variables has been studied for the open ocean using observations and models, but less is known about the variations in the coastal ocean due to observational gaps and the more complex environments. In this work, we use a Bayesian-neural-network approach to reconstruct surface carbonate chemistry variables for the Mid-Atlantic Bight (MAB) and the South Atlantic Bight (SAB) along the North American East Coast from 1982 to 2015. The reconstructed monthly time series data suggest that the rate of $f\text{CO}_2$ increase in the MAB ($18 \pm 1 \mu\text{atm}$ per decade) is faster than those in the SAB ($14 \pm 1 \mu\text{atm}$ per decade) and the open ocean ($14 \pm 1 \mu\text{atm}$ per decade). Correspondingly, pH decreases faster in the MAB. The observed stagnation in the aragonite saturation state, Ω_{arag} decrease during 2005–2015 in the MAB, is attributed to the intrusion of water from southern and offshore regions with high Ω_{arag} , which offsets the decrease expected from anthropogenic CO₂ uptake. Furthermore, seasonal asymmetry in the evolution of long-term change leads to the faster change in the amplitudes of the seasonal cycle in carbonate chemistry variables in coastal waters than those in the open ocean. In particular, the increase in the seasonal-cycle amplitude of dissolved inorganic carbon in the MAB is 2.9 times larger than that of the open ocean. This leads to the faster increase in the season-cycle amplitude of Ω_{arag} and earlier occurrence of undersaturation in coastal waters as acidification continues.

Plain Language Summary Human activities, primarily fossil fuel burning, have increased the amount of carbon dioxide in the atmosphere and absorbed by the ocean. The excess carbon dioxide absorbed by the ocean leads to ocean acidification. Coastal acidification along the North American East Coast is not well understood due to limited spatial and temporal observations and because other factors besides atmospheric uptake affect coastal acidification. In this study, we use a machine learning approach to recognize the surface water carbon chemistry patterns in the Mid-Atlantic Bight and the South Atlantic Bight, which are two coastal regions of eastern North America, and then use the trained algorithms to fill in the large observational gaps. The reconstructed time series data show that the pH of coastal water in the Mid-Atlantic Bight was lower and the rate of acidification was faster than that of the South Atlantic Bight. The rate of surface water acidification was faster in winter when pH was the lowest, thereby exerting more stress on shell-building organisms in the Mid-Atlantic Bight.

1. Introduction

The carbonate system equilibrium is the major buffer mechanism in regulating seawater pH and calcium carbonate saturation state with respect to aragonite (Ω_{arag}). Anthropogenic carbon dioxide (CO₂) emitted to the atmosphere from human activities, primarily fossil fuel burning, increases the amount of CO₂ absorbed by the ocean and leads to ocean acidification (OA, Doney et al., 2009; Orr et al., 2005). In addition to absorption of excess CO₂, upwelling, eutrophication, and river discharge affect carbonate chemistry in coastal waters and contribute to coastal acidification (Cai et al., 2011; Feely et al., 2008; Vargas et al., 2016; Wallace et al., 2014). Localized and regional acidification of coastal waters is not well understood due to its complexity and limited spatial and temporal observations and model estimates (Hofmann et al., 2011; Strong et al., 2014).

The North American East Coast is a passive continental margin that characterized by a broad shallow shelf. The cold Labrador Current and the warm Gulf Stream are two major current systems that affect the shelf water dynamics. The Labrador Current flows southward along the east coast of Nova Scotia and the Gulf

©2020. The Authors.

This is an open access article under the terms of the Creative Commons Attribution License, which permits use, distribution and reproduction in any medium, provided the original work is properly cited.

of Maine to the New York Bight (Bailey & Hachey, 1951). It transports the fresher and colder water into the Mid-Atlantic Bight (MAB) (Chapman & Beardsley, 1989) and has low Ω_{arag} and total alkalinity (TA) (Cai et al., 2020). The Gulf Stream flows northward parallel to the coast and separates from shelf water regions near Cape Hatteras. It is warm and salty and has high Ω_{arag} and TA (Cai et al., 2020). It strongly affects the shelf water dynamics along its propagation pathway in the South Atlantic Bight (SAB) (Atkinson et al., 1983; Lee et al., 1991). The CO_2 buffering capacity is low in the Labrador Current but high in the Gulf Stream.

Spatial and seasonal variabilities of seawater carbon dioxide partial pressure ($p\text{CO}_2$) have been studied in the MAB and the SAB (DeGrandpre et al., 2002; Jiang et al., 2008). The seasonal cycle of $p\text{CO}_2$ follows the seasonal thermal cycle in the SAB (Jiang et al., 2008; Signorini et al., 2013). In the MAB, biological production events partially counteract the thermally induced $p\text{CO}_2$ increase during spring and summer but they do not seriously alter the overall seasonality because stratification inhibits nutrient supply to the surface water (DeGrandpre et al., 2002). Long-term changes of carbonate chemistry have not been studied in the MAB and the SAB, despite their ecological and economic significance (Clonley et al., 2015; Goldsmith et al., 2019).

Assessment of the long-term changes of carbonate chemistry variables is essential to understand responses to anthropogenic CO_2 increase. Many continental shelves are hypothesized to be increasing carbon sinks for atmospheric CO_2 as a result of a faster exchange of CO_2 with the ocean interior and increased biological production due to an increase in anthropogenic nutrient inputs (Laruelle et al., 2018). However, other factors can counteract these processes. For instance, the OA signal in the Gulf of Maine is absent in the recent three decades as a result of rapid warming and salinity changes, which have a strong impact on the carbonate system (Salisbury & Jönsson, 2018).

It is important to examine the long-term changes in the seasonal-cycle amplitudes of carbonate chemistry parameters because it matters when calcifying species are exposed to calcium carbonate undersaturation (Gruber et al., 2002; Kwiatkowski & Orr, 2018; Sasse et al., 2015). It affects the time of emergence for OA-related parameters. It is the estimated time for OA signal to be greater than its natural variability (Salisbury & Jönsson, 2018; Turk et al., 2019). Studies on the increasing seasonal-cycle amplitudes of carbonate chemistry parameters have recently been performed (Fassbender et al., 2018; Kwiatkowski & Orr, 2018; Landschützer et al., 2018). Based on interpolated monthly sea surface $p\text{CO}_2$ for the open ocean, Landschützer et al. (2017) show that rising ocean temperatures and anthropogenic CO_2 concentration have altered the seasonal-cycle amplitudes of carbonate chemistry parameters that are attributed to warming and decreases in buffer capacity.

Long-term monthly data sets are not available for coastal regions such as the MAB and the SAB due to sparsity of $p\text{CO}_2$ observations. To address this issue, we developed algorithms for regional sea surface fugacity of carbon dioxide ($f\text{CO}_2$) from 1982 through 2015 using atmospheric CO_2 , sea surface temperature (SST), and sea surface salinity (SSS), which are the most readily available parameters, using a Bayesian-neural-network approach. Note that $p\text{CO}_2$ and $f\text{CO}_2$ are interchangeable with knowledge of temperature, surface atmospheric pressure, and hydrostatic pressure (Orr et al., 2015; Weiss, 1974). In this work, we use $f\text{CO}_2$ because it accounts for the nonideal behavior of CO_2 gas. In addition, the observations used in this work are reported in the format of $f\text{CO}_2$. The monthly interpolated sea surface $f\text{CO}_2$ is reconstructed from the available monthly atmospheric CO_2 , SST, and SSS. Other carbonate chemistry parameters, such as pH, dissolved inorganic carbon (DIC), and Ω_{arag} , are then calculated using the monthly interpolated $f\text{CO}_2$ and salinity-derived TA. The long-term changes in the annual mean and seasonal-cycle amplitude of carbonate chemistry parameters based on these reconstructed monthly time series data are presented.

2. Methods

2.1. Gridded In Situ $f\text{CO}_2$ Observations, Atmospheric CO_2 , Temperature, and Salinity

Gridded seawater $f\text{CO}_2$ observations are from the global database Surface Ocean CO_2 Atlas (SOCAT, <http://www.socat.info>) version 6. The gridded SOCAT version provides fugacity of carbon dioxide ($f\text{CO}_2$) data with a $1^\circ \times 1^\circ$ resolution in space and a monthly resolution in time from 1957 to 2017 for the global oceans and coastal seas. There are 0.3 million quality-controlled measurements in the MAB and 0.1 million quality-controlled measurements in the SAB that translates into 939 unique gridded monthly data points

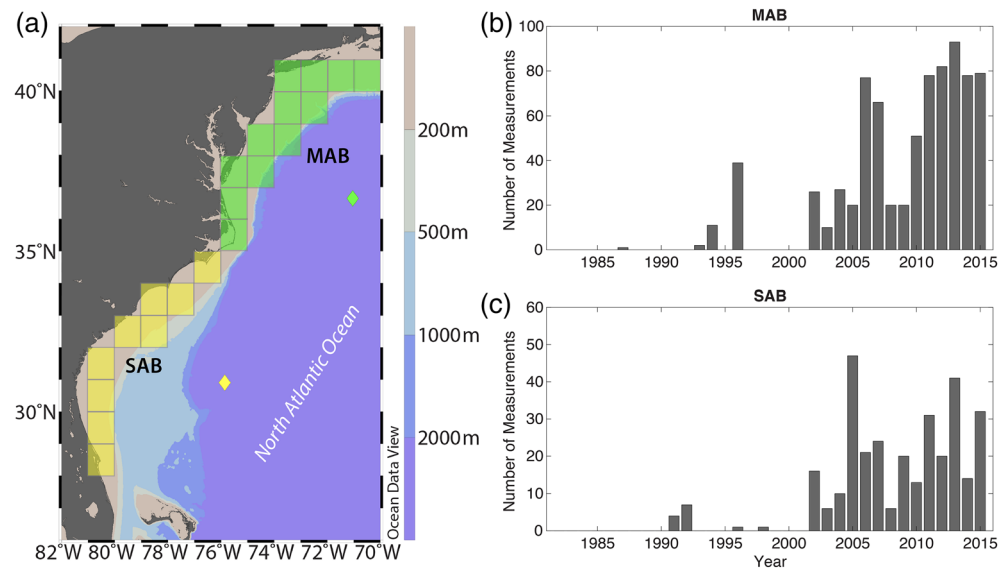


Figure 1. (a) The map of MAB and SAB with grids (rectangles, green for the MAB and yellow for the SAB). The two diamond symbols represent the open ocean points. The color bar represents ocean bathymetry. (b and c) Number of quality-controlled $f\text{CO}_2$ measurements (monthly gridded at $1^\circ \times 1^\circ$) over time in the MAB and the SAB.

for the MAB and 355 for the SAB. The number of measurements for each year and the percentage of grid cells with observations is shown in Figures 1b and 1c. Despite the large number of measurements, the number of grid boxes with data is low and it is clear that a robust gap filling method as performed here is critical. This quality-controlled product of surface ocean $f\text{CO}_2$ has an estimated accuracy of better than $5 \mu\text{atm}$ (Bakker et al., 2016).

Monthly interpolated sea surface $f\text{CO}_2$ from 1982 through 2015 is estimated from monthly atmospheric CO_2 , temperature, and salinity. Atmospheric CO_2 data come from CarbonTracker, version CT2017 (<http://carbontracker.noaa.gov>, Peters et al., 2007), which is a data assimilation system that is built by the National Oceanic and Atmospheric Administration's (NOAA) Earth System Research Laboratory (Peters et al., 2007). It provides CO_2 mole fractions with a time resolution of 3 h and spatial resolution of $1^\circ \times 1^\circ$ for North America and adjacent coastal seas from 2000 to 2015. This CO_2 mole fraction product has an accuracy of 0.1 parts per million (Peters et al., 2007). To extend the temporal coverage back to 1982, we first calculate the average monthly difference between CarbonTracker data and the Mauna Loa CO_2 data (<https://www.esrl.noaa.gov/gmd/ccgg/trends/data.html>) for each grid box using data during the overlap period (2000–2015). The CO_2 differences are generally large in summer and small in winter (supporting information Figure S1). Spatially, the CO_2 differences are larger in the higher latitudes than that in the lower latitudes (supporting information Figure S1). Then we apply this difference that ranges from -3.9 to $15.8 \mu\text{atm}$ to other years (1982–1999) when the CarbonTracker data are not available. The accuracy of the CO_2 measurements at the Mauna Loa Observatory is generally better than 0.2 ppm.

SST data are obtained from the NOAA daily Optimum Interpolation SST (OISST, version 2; Reynolds et al., 2007). OISST is a satellite-derived high-resolution ($0.25^\circ \times 0.25^\circ$) data set with an uncertainty of 0.02°C (Reynolds et al., 2002). The average temperature differences between OISST and SOCAT gridded data are $0.74 \pm 1.45^\circ\text{C}$ and $1.57 \pm 2.72^\circ\text{C}$ for the MAB and the SAB, respectively. SSS is obtained from the UK Met Office Hadley Center EN4 data set (version 4.2.1, <https://www.metoffice.gov.uk/hadobs/en4/>). The EN4 data set uses the World Ocean Database 2009 (WOD09) as its main data source (Good et al., 2013). Data from the Global Temperature and Salinity Profile Program since 1990 have been ingested into the EN4 data set (Good et al., 2013). This EN4 data set provides monthly-based $1^\circ \times 1^\circ$ gridded salinity data with uncertainty estimates. The average salinity uncertainties are 0.48 and 0.58 for the MAB and the SAB, respectively. The average salinity differences between EN4 data and SOCAT gridded data are 0.10 ± 0.68 and 0.10 ± 0.85 for the MAB and the SAB, respectively.

2.2. $f\text{CO}_2$ Estimation and pH, DIC, and Ω_{arag} Calculation

Monthly seawater $f\text{CO}_2$ at the equilibrium state ($f\text{CO}_{2\text{air}}$) is calculated using atmospheric dry air mole fraction of CO_2 ($x\text{CO}_2$), SST, and SSS for each $1^\circ \times 1^\circ$ grid box in the MAB and the SAB (Figure 1a). The equilibrium state refers to the condition that the seawater $f\text{CO}_2$ is in equilibrium with the atmospheric $f\text{CO}_2$ at 100% relative humidity and one standard atmospheric pressure, that is, the net CO_2 exchange between atmosphere and seawater is zero. $p\text{CO}_2$ at the equilibrium state ($p\text{CO}_{2\text{air}}$) is calculated using $x\text{CO}_2$, temperature, and salinity:

$$p\text{CO}_{2\text{air}} = x\text{CO}_2 \times (1 - p_w), \quad (1)$$

where p_w stands for water vapor pressure at the equilibrium temperature and salinity. It can be calculated from temperature and salinity according to Weiss and Price (1980):

$$p_w = \exp(24.4543 - 67.4509 \times (100/T) - 4.8489 \times \ln(T/100) - 0.000544 \times S), \quad (2)$$

where T is temperature on the Kelvin scale and S is salinity. Then we converted $p\text{CO}_{2\text{air}}$ to $f\text{CO}_{2\text{air}}$ using CO_2 coefficients from Weiss (1974), where for surface waters $f\text{CO}_2 \approx 0.996 p\text{CO}_2$. For consistency, we use $f\text{CO}_2$ through the paper from here.

Then we model the disequilibrium between the observed seawater $f\text{CO}_2$ and $f\text{CO}_{2\text{air}}$ (i.e., $\Delta f\text{CO}_2$; $\Delta f\text{CO}_2 = f\text{CO}_2 - f\text{CO}_{2\text{air}}$) using atmospheric CO_2 , SST, and SSS via a Bayesian-neural-network approach, which provides a way to model the nonlinear behavior of the carbonate chemistry variables with probability distribution as weights and has better performance than that of traditional empirical approaches such as the multiple linear regression approach (Bittig et al., 2018; Chen et al., 2019; MacKay, 1995). The input parameters are latitude, longitude, SST, and SSS. These four input parameters are chosen because they are commonly measured with high accuracy. Monthly SST and SSS data available from 1982 to 2015 are used to calculate output with the trained network to fill in SOCAT data gaps. The Bayesian-neural-network approach takes full usage of available observations because it obviates the overfitting problem with regularization coefficients, and thus, a subset of data for the cross validation is not necessary (Neal, 1996). In addition, it exhibits robustness to errors in the input parameters (Aires et al., 2004; Velazco et al., 1997), which is important for this study as the input parameters SST and SSS come from gridded data product with errors (section 2.1). The output parameter is $\Delta f\text{CO}_2$. The feedforward backpropagation network is constructed by two hidden layers with tanh activation functions, which provide the neural network a nonlinear element. The neural network is trained with the Levenberg-Marquardt algorithm (Hagan & Menhaj, 1994). The monthly gridded SOCAT $f\text{CO}_2$ data, along with the corresponding $f\text{CO}_{2\text{air}}$, latitude, longitude, SST, and SSS, have been used to train the network. Two separate training processes have been performed for the MAB and the SAB with 935 and 355 examples in the training data sets, respectively.

Based on the trained algorithms, monthly $\Delta f\text{CO}_2$ over 1982–2015 is calculated from monthly atmospheric CO_2 , SST, and SSS. Subsequently, monthly $f\text{CO}_2$ is calculated using $\Delta f\text{CO}_2$ and $f\text{CO}_{2\text{air}}$ according to $f\text{CO}_2 = \Delta f\text{CO}_2 + f\text{CO}_{2\text{air}}$. Monthly pH, DIC, and Ω_{arag} are then calculated from $f\text{CO}_2$ and salinity-derived TA using CO2SYS (Van Heuven et al., 2009) with the first and second dissociation constants of carbonic acid in seawater (K_1 and K_2) from Lueker et al. (2000) and borate-to-salinity ratio determined by Uppström (1974). TA is derived from salinity using linear relationships; for the MAB, $\text{TA} = 46.6 \times \text{salinity} + (670.6 \pm 12.3)$; and for the SAB, $\text{TA} = 48.7 \times \text{salinity} + (608.8 \pm 28.2)$ (Cai et al., 2010).

The salinity-TA relationships obtained in Cai et al. (2010) were obtained from high-quality cruise data before 2010 for the entire MAB and the SAB. Changes in the relationship between salinity and TA would affect the estimated TA and thus affect the calculated pH, DIC, and Ω_{arag} . To assess the influence on the results, we applied two different salinity-TA relationships for the MAB and the SAB using more recent observations and then compared the new results with the previous results using salinity-TA relationships from Cai et al. (2010). For the MAB, the new relationship of $\text{TA} = 48.96 \times \text{salinity} + 599.54$ ($n = 185$, $r^2 = 0.95$, $p < 0.05$) was developed using bottle TA data measured during the first East Coast Ocean Acidification cruise (ECO-A-1) that was conducted in 2015, which is an independent data set that was not used by Cai et al. (2010). For the SAB, a new relationship of $\text{TA} = 46.56 \times \text{salinity} + 688.24$ ($n = 892$, $r^2 = 0.93$, $p < 0.05$) was developed using TA measurements from Cai's lab for the entire SAB shelf from 2006 through 2017. The salinity-TA

relationship fitted for the SAB using ECOA-1 data was not used due to the lack of low salinity bottle samples for the SAB during this survey.

The average salinity-derived TA differences from the two sets of equations are 5.9 ± 1.9 and $3.6 \pm 1.1 \mu\text{mol kg}^{-1}$ for the MAB and the SAB, respectively. The salinity-derived TA using new equations are higher than those using previous equations with up to $10.5 \mu\text{mol kg}^{-1}$ for the MAB and up to $6.5 \mu\text{mol kg}^{-1}$ for the SAB (supporting information Figure S2). This leads to a higher DIC of up to $9.3 \mu\text{mol kg}^{-1}$ for the MAB and a higher DIC of up to $5.7 \mu\text{mol kg}^{-1}$ for the SAB. The corresponding influences on the calculated pH and Ω_{arag} are much smaller as these parameters are more strongly dependent on $f\text{CO}_2$. The pH differences vary between -0.0016 and 0.0020 in the MAB and vary between 0.0000 and 0.0011 in the SAB, which are smaller than pH measurement uncertainties. Ω_{arag} differences vary between -0.0102 and 0.0147 in the MAB and vary between 0.0000 and 0.0130 in the SAB. As for seasonal-cycle amplitudes, the influence of using different equations on pH and Ω_{arag} is very small while it is a bit larger on DIC (supporting information Figure S3). Importantly, in terms of long-term trends for all parameters (TA, DIC, pH, and Ω_{arag}), the usage of different equations has negligible influences as the changes in the long-term trends are smaller than uncertainties (supporting information Table S1).

In addition, we compare the carbonate chemistry variables in the MAB and the SAB with the values in the open ocean. We choose two grid cells (at 36.5°N , -71.5°W and 30.5°N , -75.5°W) in the north Atlantic Ocean at the latitudinal ranges of the MAB and the SAB for comparison (Figure 1a). The open ocean $f\text{CO}_2$ is obtained from the interpolated monthly surface $f\text{CO}_2$ from Landschützer et al. (2017). TA for the open ocean is determined using the locally interpolated alkalinity regression method (Carter et al., 2018). Then pH, DIC, and Ω_{arag} are calculated from $f\text{CO}_2$ and TA using the same approach as for their coastal-ocean counterparts.

Seasonal-cycle amplitude for each year from 1982 to 2015 is calculated as the difference between summer (July, August, and September) and winter (January, February, and March) means when the carbonate chemistry variables reach their maximum or minimum values within a certain year following Landschützer et al. (2018). In this work, we use the letter “A” to denote the seasonal-cycle amplitude of a carbonate chemistry variable. The average monthly seawater $f\text{CO}_2$ in the MAB generally reaches the maximum in summer and reaches the minimum in winter; thus, the seasonal-cycle amplitude of $f\text{CO}_2$ ($A_{f\text{CO}_2}$) is calculated as

$$A_{f\text{CO}_2} = (f\text{CO}_{2\text{Jul}} + f\text{CO}_{2\text{Aug}} + f\text{CO}_{2\text{Sep}})/3 - (f\text{CO}_{2\text{Jan}} + f\text{CO}_{2\text{Feb}} + f\text{CO}_{2\text{Mar}})/3. \quad (3)$$

In this work, we reconstruct surface carbonate chemistry variables starting from 1982 for two reasons: (1) $f\text{CO}_2$ is very sensitive to temperature (Takahashi et al., 2006) and the available high-resolution and high-quality SST data are from OISST version 2, which started in December 1981; (2) the gridded open ocean data for carbonate chemistry variables provided by Landschützer et al. (2017) started in 1982. Therefore, although quality-controlled $f\text{CO}_2$ measurements are not available prior to 1987 and 1991 for the MAB and the SAB (Figure 1b), respectively, we extrapolated data to 1982 to fully use the available SST data and to provide estimations for carbonate chemistry variables from 1982 to 1990. In addition, the long-term trends during 1991–2015 are provided along with the trends during 1982–2015 in supporting information Table S2.

2.3. First-Order Taylor-Series Deconvolution of Ω_{arag}

Ω_{arag} refers to the saturation state of seawater with respect to carbonate mineral aragonite, which is the second most abundant mineral form of calcium carbonate in the ocean and is more soluble than the most abundant form, calcite. By definition, Ω_{arag} is calculated as the product of the concentrations of calcium ions (Ca^{2+}) and carbonate ions (CO_3^{2-}) in seawater divided by the stoichiometric solubility product of the aragonite mineral (K_{sp}). It affects the health of carbonate bearing organisms and has often been used as an indicator for OA (Feely et al., 2008; Harris et al., 2013).

To investigate the cause of seasonal and decadal changes in Ω_{arag} , a first-order Taylor-series deconvolution approach has been used following Kwiatkowski and Orr (2018):

$$\Delta\Omega_{\text{arag}} = \left(\frac{\partial\Omega_{\text{arag}}}{\partial\text{DIC}}\right)\Delta\text{DIC} + \left(\frac{\partial\Omega_{\text{arag}}}{\partial\text{TA}}\right)\Delta\text{TA} + \left(\frac{\partial\Omega_{\text{arag}}}{\partial\text{SST}}\right)\Delta\text{SST} + \left(\frac{\partial\Omega_{\text{arag}}}{\partial\text{SSS}}\right)\Delta\text{SSS}, \quad (4)$$

where $\Delta\Omega_{\text{arag}}$ is the change in Ω_{arag} while ΔDIC , ΔTA , ΔSST , and ΔSSS are corresponding changes in

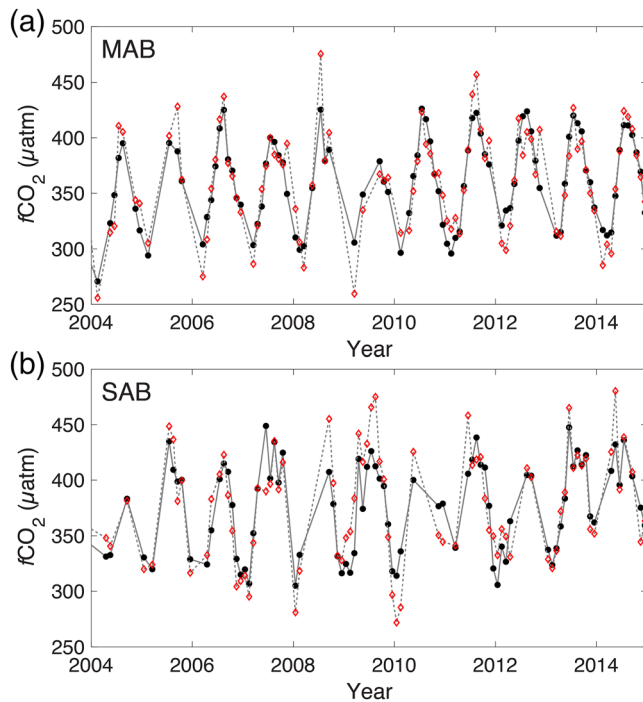


Figure 2. Time series plots of $f\text{CO}_2$ estimations and observations for the MAB (a) and the SAB (b). The black dots represent the observed $f\text{CO}_2$. The red diamond symbol represents our estimated $f\text{CO}_2$. This comparison is based on data from grid boxes where SOCAT gridded data are available and not the average of data from all grid boxes. Note that data from 1982 to 2004 are not presented here because of data paucity (Figures 1b and 1c).

DIC, TA, SST, and SSS. The four input variables, DIC, TA, SST, and SSS, can constrain the entire carbonate chemistry system. DIC and TA are chosen because they are state variables, independent of SST, while influence of SSS change on Ω_{arag} by changing equilibrium constants is small. The average derivative values ($\pm 1\sigma$) are $-0.0098 (\pm 0.0000)$, $0.0102 (\pm 0.0001)$, $0.0138 (\pm 0.0002)$, and $-0.0256 (\pm 0.0001)$, for $\frac{\partial \Omega_{\text{arag}}}{\partial \text{DIC}}$, $\frac{\partial \Omega_{\text{arag}}}{\partial \text{TA}}$, $\frac{\partial \Omega_{\text{arag}}}{\partial \text{SST}}$, and $\frac{\partial \Omega_{\text{arag}}}{\partial \text{SSS}}$, respectively.

3. Results

3.1. Regional Algorithm Performance

Figures 2 and 3a and 3b show the comparison between the neural-network-based $f\text{CO}_2$ estimations and observations. Note that the gridded data at $1^\circ \times 1^\circ$ spatial resolution from the same region (i.e., the MAB or the SAB) have been averaged to represent the values for the MAB and the SAB. Thus, the numbers of points in Figures 2 and 3 are smaller than the numbers of observations used for neural-network training. Statistically, the neural-network-based $f\text{CO}_2$ estimations agree well with gridded observations with a R^2 of 0.83 for the MAB and a R^2 of 0.82 for the SAB. The root-mean-square errors (RMSE) between gridded observations and neural-network-based estimates are 18 and 22 μatm for the MAB and the SAB, respectively. These $f\text{CO}_2$ estimates have lower RMSE of 51% and 19%, compared to previous multiple linear regression work by Signorini et al. (2013) that showed RMSE of 37 and 27 μatm for the MAB and the SAB, respectively. Compared to the MAB, the larger error in the SAB is primarily due to the poor fit of data in the grid box located in shelf regions nearest to the coast of Georgia, where seawater $f\text{CO}_2$ is affected by estuaries that have high CO_2 inputs from rivers and intertidal saltmarshes (Jiang et al., 2008).

Figures 3c–3h show the comparison between pH, DIC, and Ω_{arag} estimations and observations. The pH, DIC, and Ω_{arag} estimations are determined from the neural-network-based $f\text{CO}_2$ estimation and salinity-derived TA, while the empirical pH, DIC, and Ω_{arag} data are calculated from the observed $f\text{CO}_2$ and salinity-derived TA. The errors in the neural-network-based $f\text{CO}_2$ estimation and salinity-derived TA lead to errors in pH, DIC, and Ω_{arag} estimations. Overall, pH, DIC, and Ω_{arag} estimations agree well with empirical data with R^2 values of 0.83 (pH), 0.96 (DIC), and 0.94 (Ω_{arag}) for the MAB and R^2 values of 0.84 (pH), 0.77 (DIC), and 0.92 (Ω_{arag}) for the SAB. The errors in pH, DIC, and Ω_{arag} estimations are determined following uncertainty propagation routines as described in Orr et al. (2018). In the MAB, the errors for pH, DIC, and Ω_{arag} estimations are 0.020, 9 $\mu\text{mol kg}^{-1}$, and 0.09, respectively. In the SAB, the errors for pH, DIC, and Ω_{arag} estimations (0.021, 12 $\mu\text{mol kg}^{-1}$, and 0.12) are slightly larger than those of the MAB due to the larger error in the $f\text{CO}_2$ estimates.

3.2. Seasonal and Decadal $f\text{CO}_2$, pH, DIC, and Ω_{arag} Variations

The reconstructed monthly carbonate chemistry variables in the MAB and the SAB from 1982 to 2015 suggest that seasonal variations of carbonate chemistry variables in the MAB were larger than those in the SAB (Figures 4–6). SST reached the maximum values in summer while SSS reached the lowest values during the summer. $f\text{CO}_2$ seasonal variability was consistent with SST seasonal variability, while DIC seasonal variability was consistent with SSS seasonal variability (Figures 5 and 6). However, $f\text{CO}_{2\text{air}}$ seasonal variation pattern was opposite to that of seawater $f\text{CO}_2$ due to the low air CO_2 values in late summer as plants absorb CO_2 through photosynthesis (Figure 5). Contrary to the seasonal variation patterns of $f\text{CO}_2$, pH displayed the opposite seasonal variation pattern as that of SST due to the inverse temperature effect on pH (Figure 5). Contrary to the seasonal variations of DIC, Ω_{arag} displayed the opposite seasonal variation patterns as that of SSS (Figure 6). Ω_{arag} was highest in summer because both temperature increase and biological uptake lead to an increase in Ω_{arag} .

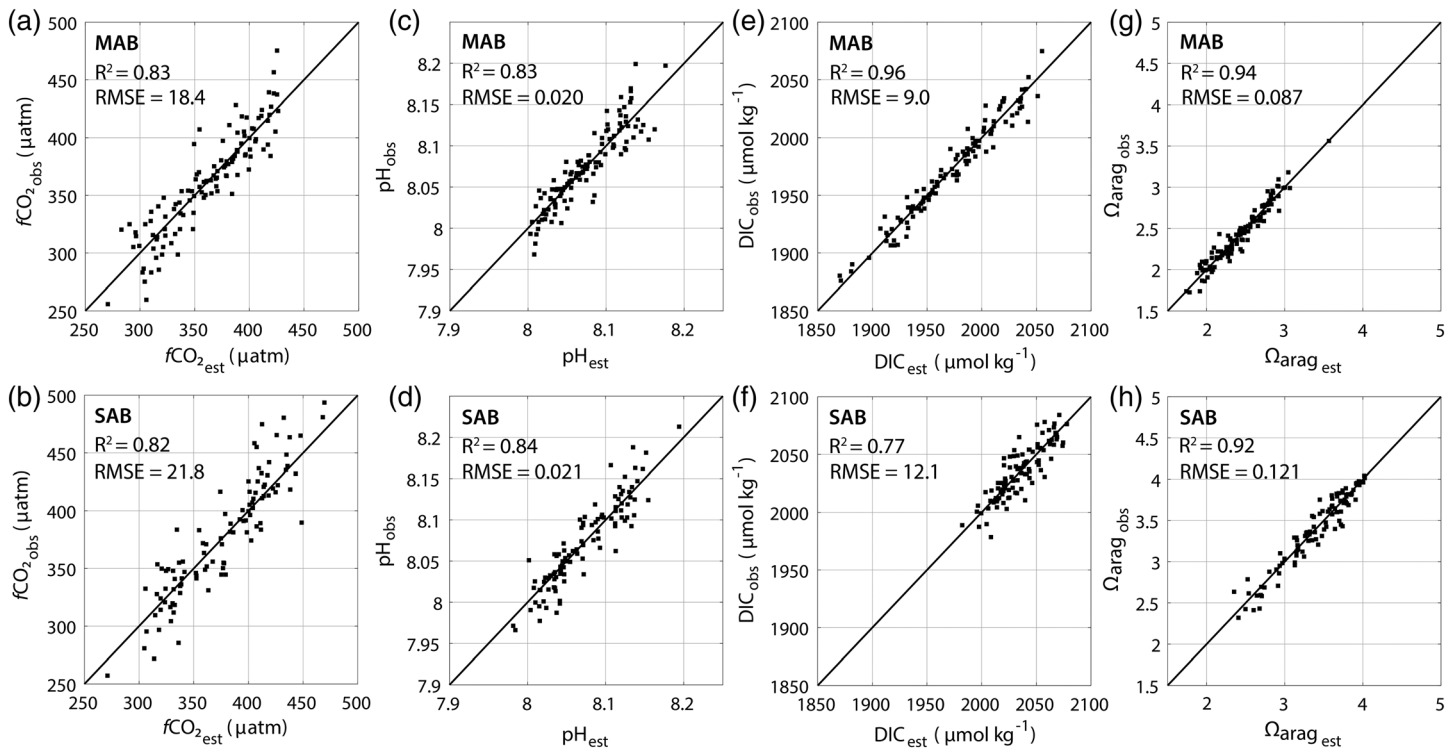


Figure 3. Scatterplots of $f\text{CO}_2$, pH, DIC, and Ω_{arag} estimations versus observations for the MAB (a, b, c, and d) and the SAB (e, f, g, and h). The black 1:1 line represents where estimation equals to observation. The R^2 values and the root-mean-square error (RMSE) of the fitted regression lines for estimations and observations are shown on each panel.

On a decadal scale, seawater $f\text{CO}_2$ increased in both the MAB and the SAB following the increase of atmospheric CO_2 (Figures 4a, 4b, and 4d). The rate of $f\text{CO}_2$ increase in the MAB ($17.7 \pm 0.7 \mu\text{atm}$ per decade, Figure 5d) was similar to that in the atmosphere ($17.3 \pm 0.2 \mu\text{atm}$ per decade) but higher than that in the SAB ($14.0 \pm 1.4 \mu\text{atm}$ per decade, Figure 5d). Correspondingly, pH decreased in both the MAB and the SAB (Figures 4c and 4d). The rate of pH decrease in the MAB (0.019 ± 0.001 per decade, Figure 5f) was higher than that in the SAB (0.013 ± 0.002 per decade, Figure 5f and Table 1).

DIC and Ω_{arag} displayed more complicated variation patterns (Figures 4 and 6). The overall DIC trends during 1982–2015 were significant in both the MAB and the SAB (Figure 6d and Table 1). For the MAB, coastal ocean DIC increased at a rate of $10.6 \pm 2.2 \mu\text{mol kg}^{-1}$ per decade during 1982–2015 (Figure 6d and Table 1). The overall DIC increase during 1982–2015 in the SAB ($12.6 \pm 1.3 \mu\text{mol kg}^{-1}$ per decade) was faster than that of the MAB, a pattern opposite that of $f\text{CO}_2$ (Figure 6d and Table 1). However, DIC in the MAB displayed different patterns during different time period. There was no significant trend in DIC from 1982 to 2005 in the MAB, but it increased from 2005 to 2015 at a rate of $39.1 \pm 8.5 \mu\text{mol kg}^{-1}$ per decade (Figure 6d and Table 1).

Different from DIC variations, the overall Ω_{arag} decrease rate in the MAB (0.103 ± 0.010 per decade, Figure 6f) was faster than that of the SAB (0.063 ± 0.015 per decade, Figure 6f and Table 1). In the MAB, contrary to DIC increase during 2005–2015, Ω_{arag} was stagnant during this period instead of decreasing caused by anthropogenic CO_2 uptake (Figure 6f and Table 1). Similarly, a recent stagnant in Ω_{arag} decrease from 2005 to 2015 was observed in the SAB (Figure 6f and Table 1).

For the open ocean, data from offshore of the MAB and the SAB displayed similar patterns in terms of both seasonal and long-term variations (Figures 5 and 6). Seasonal and long-term variations of carbonate chemistry variables in the open ocean were closer to those in the SAB than those in the MAB (Figures 5 and 6, and Table 1). In addition, Ω_{arag} in the open ocean was much higher (1.14 on average) than that in the MAB (Figures 6e and 6f, and Table 1). Specifically, $f\text{CO}_2$ increased at rates of 14.4 ± 0.5 and $13.8 \pm 0.4 \mu\text{atm}$ per decade in the open ocean at the counterparts of the MAB and the SAB during 1982–2015.

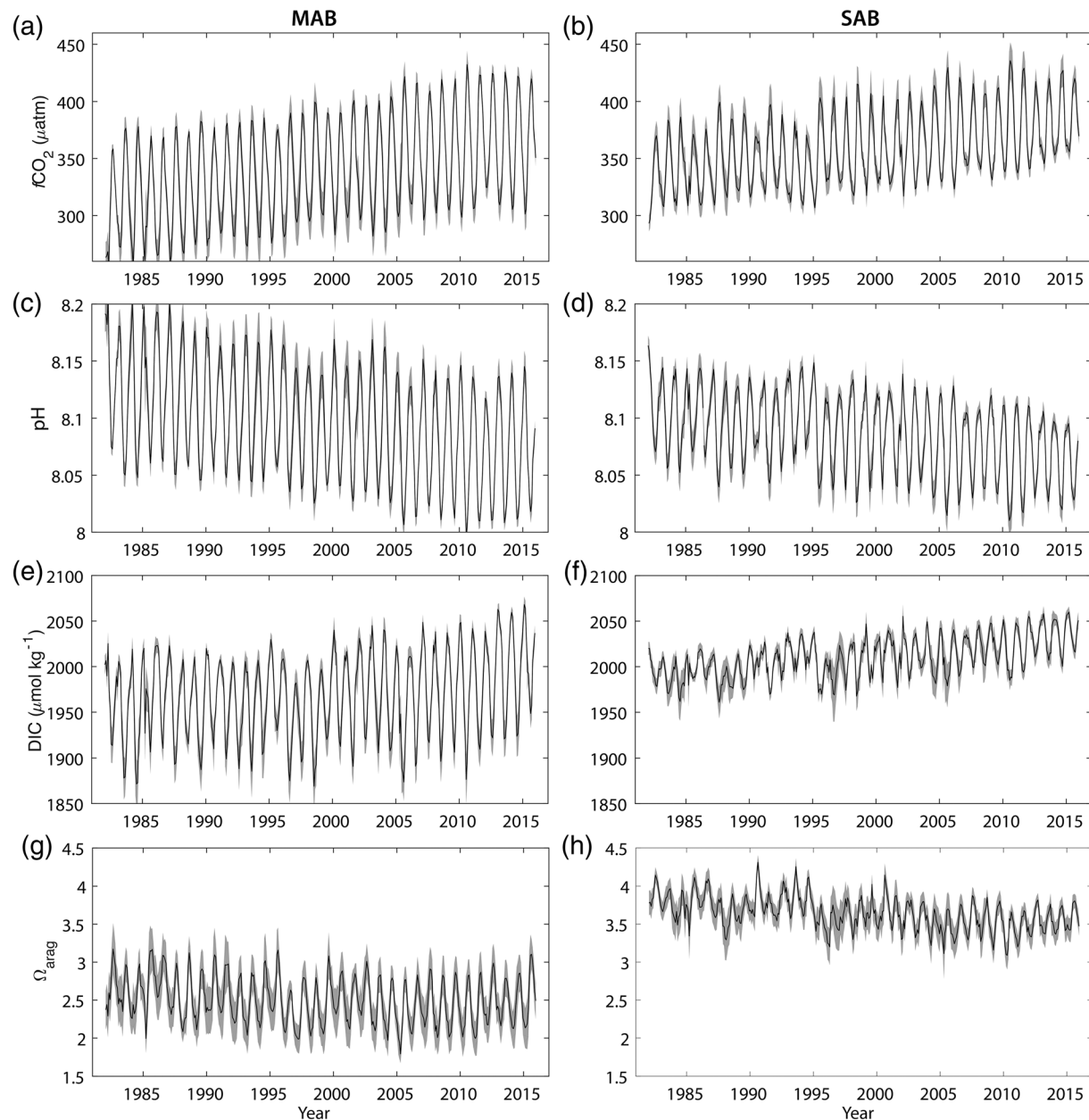


Figure 4. $f\text{CO}_2$, DIC, pH, and Ω_{arag} reconstruction for the MAB (left column) and the SAB (right column). The black line represents monthly data. The gray shade represents one standard deviation of the monthly data (i.e., monthly spatial variation). The climatological spatial distributions of $f\text{CO}_2$, DIC, pH, and Ω_{arag} are provided in supporting information Figure S11.

Correspondingly, pH decreased at rates of 0.015 ± 0.004 and 0.013 ± 0.005 per decade; DIC increased at rates of 4.9 ± 2.3 and $8.9 \pm 2.0 \mu\text{mol kg}^{-1}$ per decade; and Ω_{arag} decreased at rates of 0.067 ± 0.015 and 0.073 ± 0.011 per decade, respectively, in the open ocean offshore of the MAB and the SAB.

3.3. Variations in Seasonal-Cycle Amplitudes of $f\text{CO}_2$, pH, DIC, and Ω_{arag}

In addition to changes in annual means, the seasonal-cycle amplitudes of $f\text{CO}_2$, pH, DIC, and Ω_{arag} were also changing during 1982–2015 (Figure 7). Note that seasonal-cycle amplitude (denoted by “A” in this paper) was calculated as the difference between summer and winter means. A periodicity of the amplitude of $f\text{CO}_2$, DIC, pH, and Ω_{arag} at about 5.5 years per cycle was presented in both the MAB and the SAB according to the frequency analysis of detrended and normalized annual anomalies in amplitude during 1982–2015 via the multitaper method (Percival & Walden, 1993; Thomson, 1982). This 5.5-year per cycle periodicity

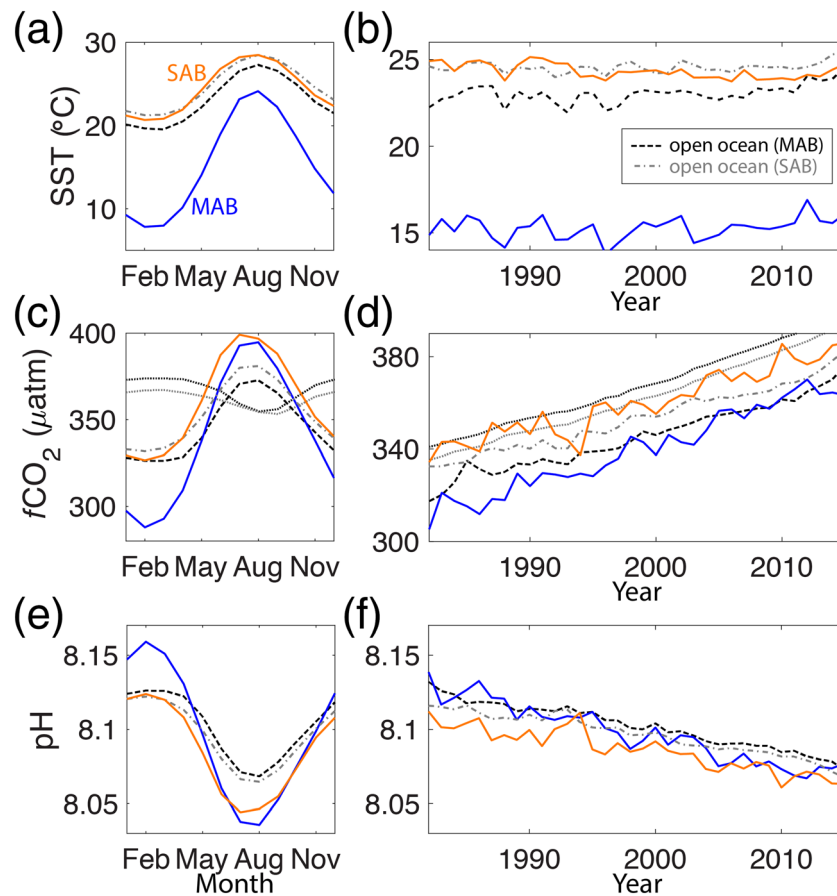


Figure 5. Seasonal (left panels, monthly data, average over 1982–2015) and decadal (right panels, annual data) SST, $f\text{CO}_2$, and pH variations in the MAB (blue) and the SAB (orange). The dashed lines represent data from the open ocean at the latitudinal ranges of the MAB (black) and the SAB (gray). In Figures 5c and 5d, the dotted lines represent $f\text{CO}_{2\text{air}}$ in the MAB (black) and the SAB (gray).

appears impacted, to a large degree, by the North Atlantic Oscillation, which shares a similar periodicity during 1982–2015 (supporting information Figures S4 and S5) and exerts a strong influence on temperature variation in the North Atlantic (Czaja & Frankignoul, 2002; Visbeck et al., 2001).

The long-term changes in the seasonal-cycle amplitudes of $f\text{CO}_2$ and pH in the MAB and the SAB were similar to those in the open ocean, though the climatological seasonal-cycle amplitudes in the coastal ocean were amplified compared to those in the open ocean (Figures 7a–7d). In the open ocean, the seasonal-cycle amplitude of $f\text{CO}_2$ of 42.7 ± 4.4 and 45.3 ± 4.8 μatm on average increased during 1982–2015 at rates of 2.8 ± 0.6 and 2.7 ± 0.7 μatm per decade, respectively, for the open-ocean counterparts of the MAB and the SAB (Figures 7a and 7b). The seasonal-cycle amplitudes of $f\text{CO}_2$ in the MAB and the SAB of 96.2 ± 8.6 and 66.1 ± 12.1 μatm increased at higher rates of 4.6 ± 1.3 and 4.0 ± 2.0 μatm per decade (Figures 7a and 7b). No significant trends were detected for the seasonal-cycle amplitude of pH in coastal or open oceans (Figures 7c and 7d). This is attributed to the pH being on a log scale. The seasonal-cycle amplitude of pH was determined by the combined effects of the seasonal-cycle amplitude of $[\text{H}^+]$ and the annual mean $[\text{H}^+]$ as pH is a log transformation of $[\text{H}^+]$ and $\text{dpH} = d(-\log[\text{H}^+]) = -2.303 \times (d[\text{H}^+]/[\text{H}^+])$ (Kwiatkowski & Orr, 2018). Thus, due to the increases in both terms, the annual mean $[\text{H}^+]$ and the seasonal-cycle amplitude of $[\text{H}^+]$ partially cancel each other and result in a smaller change or no change in the seasonal-cycle amplitude of pH.

The changes in the seasonal-cycle amplitudes of DIC and Ω_{arag} in the MAB were significantly different from those in the open ocean (Figures 7e–7h). The seasonal-cycle amplitude of DIC of 56.8 ± 19.3 $\mu\text{mol kg}^{-1}$ increased (not statistically significant, p value = 0.35) at a rate of 3.2 ± 3.4 $\mu\text{mol kg}^{-1}$ per decade in the open ocean while the seasonal-cycle amplitude of the MAB of 101.0 ± 17.8 $\mu\text{mol kg}^{-1}$ increased much faster at a rate of 8.9 ± 2.7 $\mu\text{mol kg}^{-1}$ per decade (p value < 0.001; Figure 7e). At the same time, the seasonal-cycle

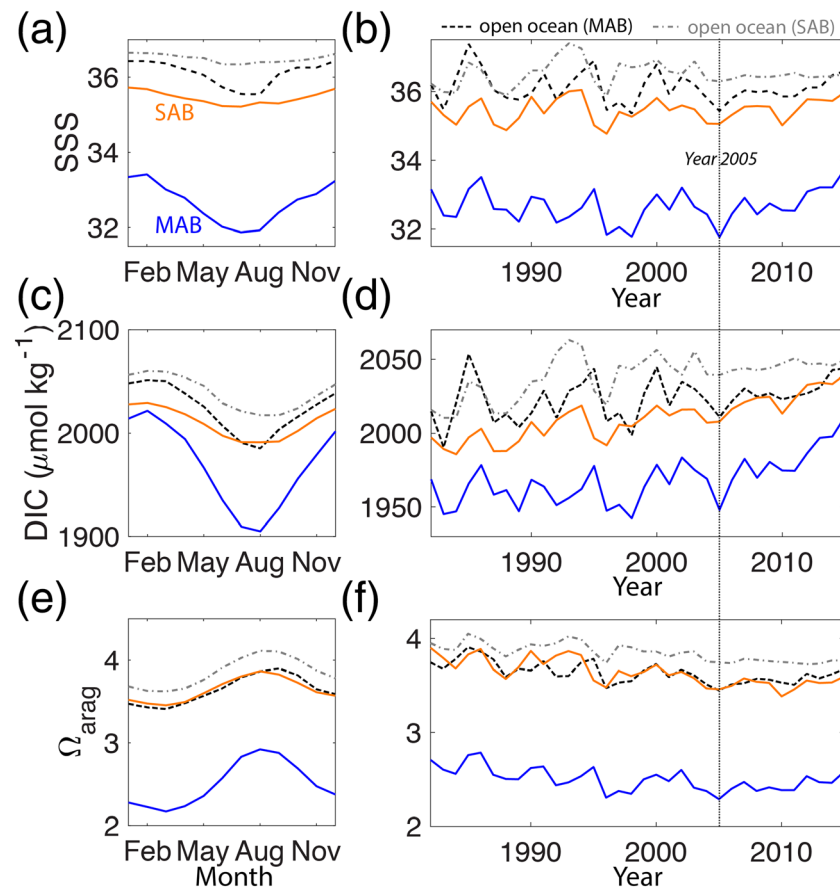


Figure 6. Seasonal (left panels, average over 1982–2015) and decadal (right panels) SSS, DIC, and Ω_{arag} variations in the MAB (blue) and the SAB (orange). The dashed lines represent data from the open ocean at the latitudinal ranges of the MAB (black) and the SAB (gray). The dotted vertical line represents year 2005 when salinity started increasing in the MAB.

amplitude of Ω_{arag} in the MAB increased (not statistically significant, p value = 0.11) at a rate of 0.034 ± 0.021 per decade while it decreased slightly (not statistically significant, p -value = 0.92) in the open ocean at a rate of 0.002 ± 0.017 per decade (Figure 7g). The seasonal-cycle amplitudes of DIC and Ω_{arag} in the SAB increased as those in the open ocean, though a significant trend was found only for the seasonal-cycle amplitude of DIC in the SAB (Figures 7f and 7h).

4. Discussion

4.1. The Influence of Atmospheric CO₂ Increase on $f\text{CO}_2$ and pH

Seasonal and interannual variabilities of carbonate chemistry variables in the open ocean have been studied (Bates et al., 1996; Gruber et al., 2002; Sasse et al., 2015). It has been concluded that the interannual variability of carbonate chemistry variables in the north Atlantic is mainly driven by variations in winter mixed-layer depths and by SST anomalies (Gruber et al., 2002). Seasonal air-sea CO₂ flux has been studied in the MAB and the SAB by DeGrandpre et al. (2002) and Signorini et al. (2013) for time periods 1994 to 2000 and 2003 to 2010, respectively. $f\text{CO}_2$ seasonal variation is most sensitive to temperature change in both the MAB and the SAB (Signorini et al., 2013). Our regional averaged seasonal $f\text{CO}_2$ also varies with SST (supporting information Figure S6). Consequently, seasonal change of $f\text{CO}_2$ in the MAB is larger than that in the SAB because seasonal temperature variation in the MAB is larger. As for pH, it varies inversely with $f\text{CO}_2$ in both the MAB and the SAB (supporting information Figure S6). Therefore, its seasonal amplitude in the MAB is larger than that in the SAB. DIC reaches the highest values in winter when the mixed layer depth is highest. From winter to summer, DIC draws down as results of CO₂ degassing and spring-summer biological activity. DIC reaches minimum in summer when stratification is strongest. From summer to fall, DIC

Table 1

Decadal Change Rates and Seasonal Amplitudes of $f\text{CO}_2$ (μatm), pH, DIC ($\mu\text{mol kg}^{-1}$), and Ω_{arag} in the MAB, the SAB, and the Open Ocean During 1982–2015 if Not Specified

		MAB	SAB	Open oceanoffshore of the MAB	Open oceanoffshore of the SAB
Decadal change of annual mean	$f\text{CO}_2$ in situ	17.7 ± 0.7	14.0 ± 0.9	14.4 ± 0.5	13.8 ± 0.4
	$f\text{CO}_2$ at 25 °C	22.9 ± 2.2	14.0 ± 0.9	11.0 ± 1.0	12.6 ± 0.5
	pH in situ	-0.019 ± 0.001	-0.013 ± 0.001	-0.015 ± 0.004	-0.013 ± 0.005
	pH at 25 °C	-0.016 ± 0.002	-0.017 ± 0.001	-0.011 ± 0.001	-0.012 ± 0.001
	DIC	10.6 ± 2.2	12.6 ± 1.3	4.9 ± 2.3	8.9 ± 2.0
	<i>DIC 1982–2005</i>	$3.5 \pm 3.6^*$	10.1 ± 2.3	$3.6 \pm 4.5^*$	14.5 ± 3.8
	<i>DIC 2005–2015</i>	39.1 ± 8.5	23.1 ± 5.6	19.2 ± 5.9	6.6 ± 2.2
	TA	$3.3 \pm 3.9^*$	$2.8 \pm 2.9^*$	$-2.5 \pm 3.7^*$	$1.6 \pm 3.1^*$
	<i>TA 1982–2005</i>	$-9.2 \pm 6.4^*$	$-1.5 \pm 5.3^*$	$-7.3 \pm 7.1^*$	$8.4 \pm 5.6^*$
	<i>TA 2005–2015</i>	39.6 ± 14.5	$19.8 \pm 14.6^*$	23.3 ± 9.3	$2.3 \pm 3.2^*$
	Ω_{arag}	-0.103 ± 0.010	-0.063 ± 0.015	-0.067 ± 0.015	-0.073 ± 0.011
	<i>Ω_{arag} 1982–2005</i>	-0.125 ± 0.030	-0.126 ± 0.031	-0.106 ± 0.028	-0.065 ± 0.021
	<i>Ω_{arag} 2005–2015</i>	$0.089 \pm 0.066^*$	$-0.007 \pm 0.080^*$	0.106 ± 0.045	$-0.025 \pm 0.025^*$
	$f\text{CO}_2$ in situ	96.2 ± 8.6	66.1 ± 12.0	42.7 ± 4.4	45.3 ± 4.8
Seasonal amplitude	pH in situ	0.110 ± 0.010	0.073 ± 0.013	0.053 ± 0.003	0.053 ± 0.005
	DIC	101.0 ± 17.8	30.0 ± 11.2	56.8 ± 19.3	39.9 ± 12.5
	Ω_{arag}	0.669 ± 0.124	0.357 ± 0.110	0.423 ± 0.099	0.430 ± 0.086
	$f\text{CO}_2$ in situ	4.6 ± 1.3	$4.0 \pm 2.0^*$	2.8 ± 0.6	2.7 ± 0.7
Decadal change of seasonal amplitude	pH in situ	$0.000 \pm 0.000^*$	$0.000 \pm 0.000^*$	0.001 ± 0.000	$0.001 \pm 0.000^*$
	DIC	8.9 ± 2.7	5.1 ± 1.8	$3.2 \pm 3.4^*$	$3.5 \pm 2.1^*$
	Ω_{arag}	$0.034 \pm 0.021^*$	$0.022 \pm 0.019^*$	$-0.002 \pm 0.017^*$	$0.015 \pm 0.015^*$

Note. The units for decadal change rates of $f\text{CO}_2$, pH, DIC ($\mu\text{mol kg}^{-1}$), and Ω_{arag} are μatm per decade, per decade, $\mu\text{mol kg}^{-1}$ per decade, and per decade, respectively.

The corresponding p value is larger than 0.05.

Italicized data illustrate a time period that is different from the entire period (1982–2015).

increases due to vertical mixing and high DIC below the mixed layer as wind becomes stronger and the mixed layer depth becomes larger. However, to what scales the surface carbonate chemistry variables are affected by subsurface carbonate chemistry dynamics are not discussed here due to the lack of subsurface carbonate chemistry data for spring, fall, and winter for the MAB.

In terms of long-term changes of seawater $f\text{CO}_2$ and pH, the in situ $f\text{CO}_2$ and pH are normalized using CO2SYS to the values at 25° to normalize for temperature influence. The temperature-normalized $f\text{CO}_2$ displays similar long-term trends as the in situ $f\text{CO}_2$ in the SAB and its offshore open ocean (supporting information Figure S7 and Table 1), suggesting that atmospheric CO_2 increase is the primary driver of the long-term $f\text{CO}_2$ increase in the SAB. However, for the MAB, the temperature-normalized $f\text{CO}_2$ and pH trends display similar patterns as the in situ $f\text{CO}_2$ and pH but somewhat different rates (supporting information Figure S7 and Table 1), suggesting that other factors, for example, salinity change and mixing, have notable influence on the long-term $f\text{CO}_2$ change in the MAB on top of the influence from atmospheric CO_2 increase. Temperature and vertical mixing have opposite influences on seawater $f\text{CO}_2$, thus counteracting each other and resulting in a similar increase rate of in situ $f\text{CO}_2$ as that of the $f\text{CO}_{2\text{air}}$. The MAB and the SAB have been identified as CO_2 sinks by DeGrandpre et al. (2002), Jiang et al. (2008), and Signorini et al. (2013). As in situ seawater $f\text{CO}_2$ increase rate in the MAB of 17.7 ± 0.7 μatm per decade is similar to $f\text{CO}_{2\text{air}}$ increase rate (17.3 ± 0.2 μatm per decade), the MAB will likely remain to be CO_2 sinks with a similar air-sea CO_2 flux rate in the next few decades. Seawater $f\text{CO}_2$ increase rate in the SAB (14.0 ± 0.7 μatm per decade) is lower than $f\text{CO}_{2\text{air}}$ increase rate (17.3 ± 0.2 μatm per decade), indicating that SAB has become a larger CO_2 sink in the last four decades (Laruelle et al., 2018).

4.2. Atmospheric CO_2 Increase and Mixing Influences on DIC

To quantify the influence of atmospheric CO_2 increase on the long-term DIC change, the simulated DIC is calculated using the detrended seawater $f\text{CO}_2$ and TA to eliminate the influence of atmospheric CO_2 increase. Then the difference between the interpolated DIC using the neural network approach and the simulated DIC represents the influence of atmospheric CO_2 increase on DIC increase. It is clear that

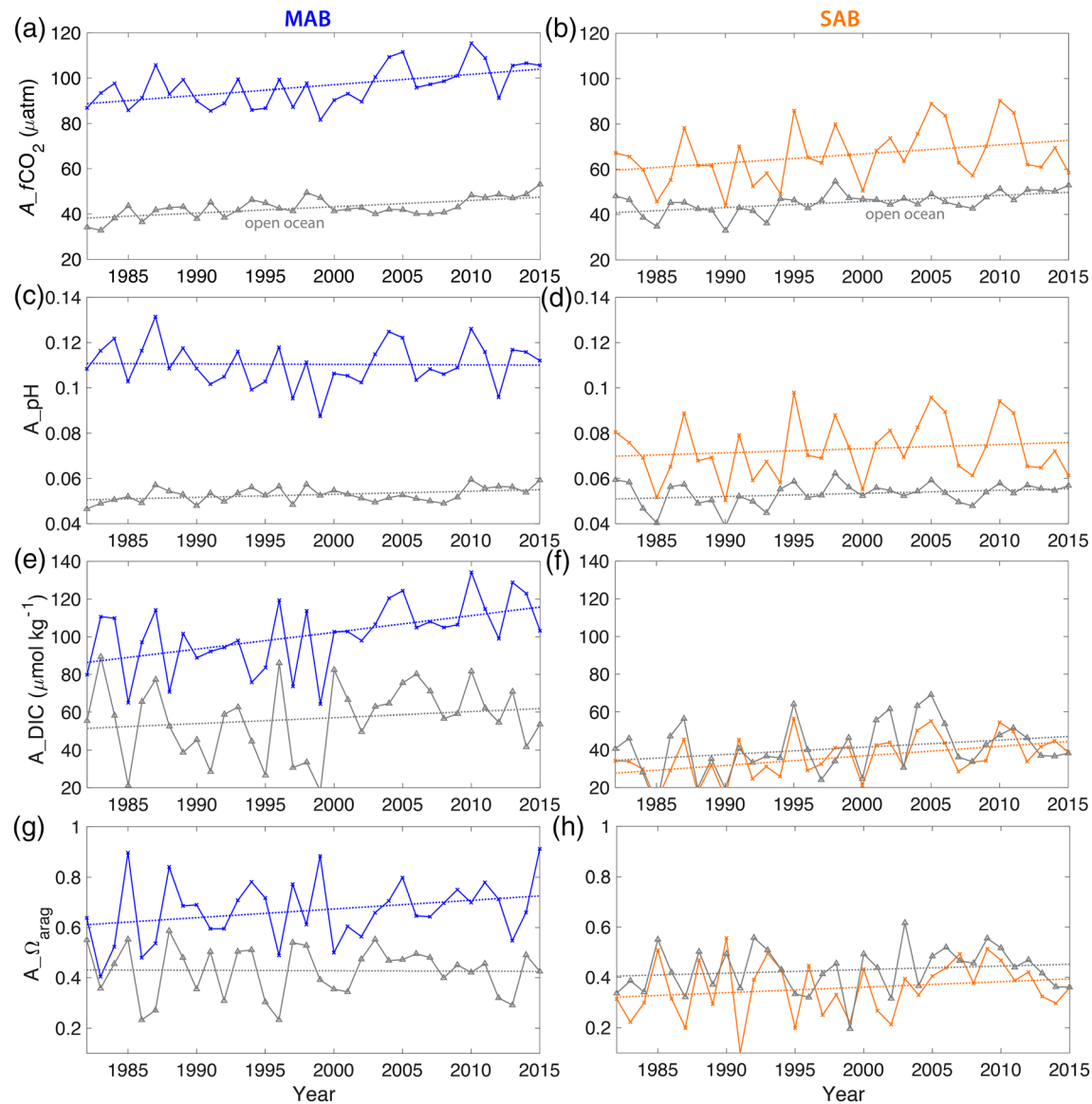


Figure 7. Changing seasonal-cycle amplitudes of $f\text{CO}_2$, pH, DIC, and Ω_{arag} in the MAB (left panels, blue) and the SAB (right panels, orange). The gray solid lines represent data from the open ocean at the latitudinal ranges of the MAB and the SAB. The dashed lines are least squares linear regression lines for each region.

atmospheric CO_2 increase contributes to DIC accumulation over time (supporting information Figure S8). DIC increase rates due to atmospheric CO_2 uptake are $0.99 \pm 0.01 \mu\text{mol kg}^{-1} \text{ year}^{-1}$ for the MAB and $0.88 \pm 0.01 \mu\text{mol kg}^{-1} \text{ year}^{-1}$ for the SAB (supporting information Figure S8c). On the other hand, the average air-sea CO_2 uptake rates are 1.91 ± 0.22 and $0.75 \pm 0.16 \text{ mol CO}_2 \text{ m}^{-2} \text{ year}^{-1}$, respectively, for the MAB and the SAB (Signorini et al., 2013). These lead to estimated CO_2 uptake of 92.8 ± 10.7 and $48.6 \pm 10.4 \mu\text{mol kg}^{-1} \text{ year}^{-1}$ assuming seawater density is $1,029 \text{ kg m}^{-3}$ and the average mixed layer depths are 20 and 15 m for the MAB and the SAB (Signorini et al., 2013). Thus, comparison of DIC increase rates derived here ($0.88\text{--}0.99 \mu\text{mol kg}^{-1} \text{ yr}^{-1}$) and from the mean annual air-sea fluxes ($48.6\text{--}92.8 \mu\text{mol kg}^{-1} \text{ year}^{-1}$) suggests most of the CO_2 uptake via air-sea CO_2 flux is exported to the subsurface water or the open ocean while 1.1% and 1.8% of the CO_2 uptake contribute to surface DIC increase in the MAB and the SAB, respectively. Furthermore, atmospheric CO_2 increase contributes the decrease in buffer capacity that contributes to the increase in the seasonal-cycle amplitude of DIC (supporting information Figure S8d). The change in buffer capacity accounts for 27% and 31% of the total increases in DIC seasonal-cycle amplitudes in the MAB and the SAB, respectively.

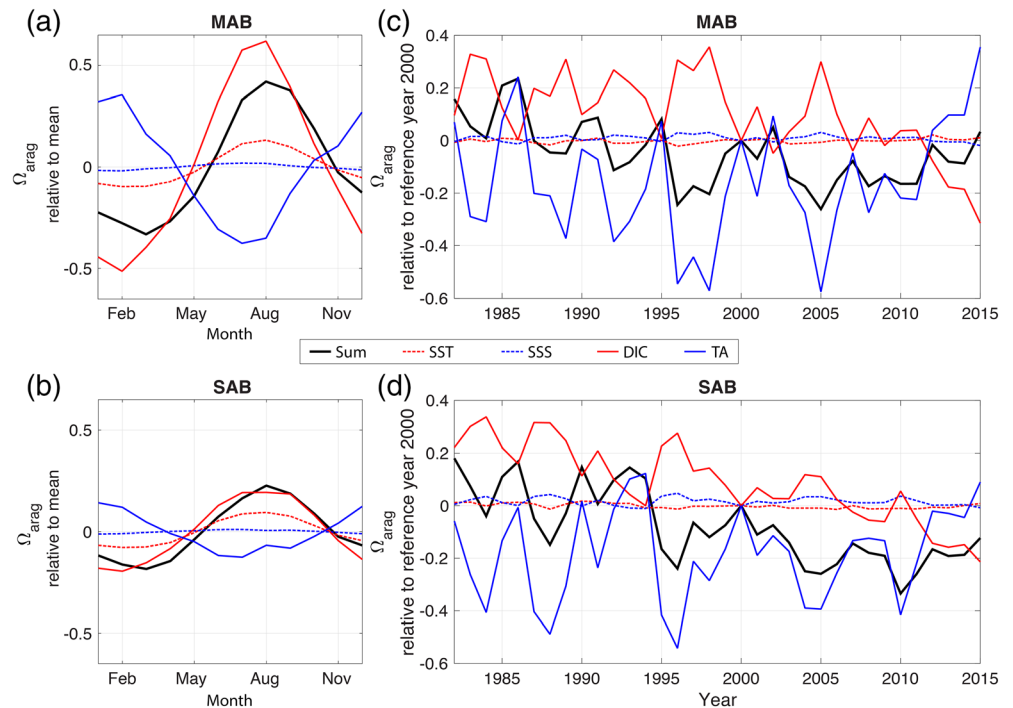


Figure 8. Factors influencing seasonal, interannual, and decadal Ω_{arag} variability in the MAB (a, c) and the SAB (b, d). The blue and red dashed line represents the partial change of Ω_{arag} contributed by the change SST, and SSS and the red and blue solid lines by the change in DIC, and TA. The solid black line represents the total change in Ω_{arag} from the four input variables.

Seasonal DIC variability in the MAB and the SAB are mainly driven by convective mixing and spring–summer biological activity that elevates DIC in winter and accounts for DIC reduction in summer (Signorini et al., 2013). To investigate DIC change on longer time scales, in situ DIC is normalized to salinity 35 using riverine and oceanic end-members for the MAB and the SAB. The interannual variability in the salinity-normalized DIC is influenced by the change in winter mixed layer depth and SST anomalies as in the north Atlantic (Gruber et al., 2002). However, the difference between the in situ DIC and salinity-normalized DIC suggests that the large DIC increase during 2005–2015 is primarily driven by the large increase in salinity as the northward movement of the latitudinal position of the Gulf Stream north wall and the retreat of the Labrador Current (supporting information Figure S7; Grodsky et al., 2017; Thomas et al., 2017).

4.3. The Cause of Seasonal, Interannual, and Decadal Changes in Ω_{arag}

Using the deconvolution method in 2.3 the seasonal variability in Ω_{arag} is investigated. The derivative values for ΔSST (0.0138 ± 0.0002) and ΔSSS (-0.0256 ± 0.0001) have opposite signs, suggesting the opposite influence on the change in Ω_{arag} . Similarly, the opposite signs in the derivative values for ΔDIC (-0.0098 ± 0.0000) and ΔTA (0.0102 ± 0.0001) suggest the opposite influence on the change in Ω_{arag} . Although the sensitivities for ΔSST and ΔSSS are larger than those for DIC and TA, seasonal Ω_{arag} variability is controlled by changes in DIC and TA to a large extent and to a lesser extent by SST in both the MAB and the SAB (Figures 8a and 8b). While SSS influence on Ω_{arag} through changing carbon system equilibrium constants is negligible (Figures 8a and 8b). This is due to the fact that the changes in DIC and TA are much larger than the changes in SST and SSS while the derivative values are on the same magnitude. For the MAB, DIC influence on seasonal Ω_{arag} variability is the largest compared to the other factors (Figures 8a and 8b). However, in terms of interannual Ω_{arag} variability, TA influence is the largest, indicating that the interannual variability is mainly controlled by physical mixing. On a decadal scale, DIC and TA are the dominant factors that control the long-term changes in Ω_{arag} (Figures 8c and 8d). In the MAB, the decrease in Ω_{arag} from 1982 to 2005 is mainly driven by the increase in DIC and the decrease in TA. However, in the recent

decade, TA increase fast in the MAB due to the increase in Gulf Stream water mass as the northward shift of the Gulf Stream north wall, which is related to zonal wind variability and North Atlantic Oscillation (Grodsky et al., 2017). Therefore, the stagnation of the Ω_{arag} trend in the recent decade is mainly driven by the larger increase in TA counteracting the effect on-going DIC increase on Ω_{arag} . In the SAB, Ω_{arag} decrease from 1982 to 2005 is mainly driven by the increase in DIC while the decadal change driven by TA is small. Similar to the MAB, the recent Ω_{arag} stagnation in the SAB is driven by the increase in TA though the increase is smaller compared to that of the MAB.

4.4. Implications of the Changes in Seasonal-Cycle Amplitude

The increase in the seasonal-cycle amplitudes of $f\text{CO}_2$ and DIC is mainly due to the increased uptake of anthropogenic CO_2 and associated reduced buffer capacity (Kwiatkowski & Orr, 2018; Landschützer et al., 2018). The greater increase of the $f\text{CO}_2$ and DIC seasonal cycle amplitudes in the MAB can be attributed to the larger CO_2 uptake through air-sea CO_2 flux than those of the SAB (Signorini et al., 2013), which lead to greater increase in seawater $f\text{CO}_2$ and DIC and greater decrease in buffer capacity. As for Ω_{arag} , the increase in its amplitude in both the MAB and the SAB is because of a higher sensitivity to the change in the seasonal amplitude of DIC than that of TA (Kwiatkowski & Orr, 2018).

Overall, the seasonal-cycle amplitudes of carbonate chemistry variables are larger in the coastal ocean than those in the open ocean. In the MAB, the average seasonal amplitudes of DIC and Ω_{arag} are higher than those in the open ocean by 160% and 175%, respectively. While the average seasonal amplitudes of DIC and Ω_{arag} in the SAB are higher than those in the offshore open ocean by 52% and 67%, respectively. The differences between the average seasonal amplitudes of DIC and Ω_{arag} in the MAB and those in the offshore open ocean of the same latitudinal range are larger compared to the differences between those in the SAB and the offshore open ocean.

The high seasonal variability of carbonate chemistry variables in the coastal ocean suggests a higher degree of vulnerability to extremes in the ongoing OA. In the MAB, surface water Ω_{arag} decreases at a rate that is 1.6 times faster in winter season, when Ω_{arag} reaches the annual minimum, than that in summer when Ω_{arag} reaches the annual maximum. This seasonal asymmetry leads to the increase in seasonal-cycle amplitude of Ω_{arag} in the MAB. This indicates a lower Ω_{arag} in winter season when Ω_{arag} reaches the annual minimum. Besides, the increase of Ω_{arag} seasonal-cycle amplitudes is greater in the MAB than those in the SAB and the open ocean. Thus, the faster increase in the seasonal amplitude of Ω_{arag} will accelerate the emergence of undersaturation in the MAB and exert more stress on coastal carbonate-bearing organisms. The current work takes the advantage of the long-term $f\text{CO}_2$ and SST data in surface waters and focus on addressing the long-term trends of $f\text{CO}_2$, pH, DIC, and Ω_{arag} and changes in their seasonal-cycle amplitudes in coastal surface waters. The Ω_{arag} is often lower in subsurface or bottom waters during stratification in the summer where most adult shelf-building organisms reside in (Saba et al., 2019).

5. Conclusion

Assessments of the long-term changes in seawater carbonate chemistry variables and their seasonal-cycle amplitudes are necessary to understand the responses of seawater carbonate chemistry to anthropogenic CO_2 uptake and to estimate when carbonate-bearing organisms will be exposed to unfavorable calcium carbonate saturation levels. Compared to open OA, coastal acidification is more difficult to investigate due to its complexity and the lack of observations. In this study, we address the coastal acidification problem using the Bayesian-neural-network approach to reconstruct $\Delta f\text{CO}_2$ and then calculate other carbonate chemistry variables at a monthly resolution for the MAB and the SAB from 1982 to 2015. The monthly interpolated data suggest that the seasonal-cycle amplitudes of carbonate chemistry variables are larger and change faster in coastal regions, especially in the MAB, than those in the open ocean. This accelerates the emergence of unfavorable conditions for coastal carbonate-bearing organisms. We found that the long-term seawater $f\text{CO}_2$, DIC, pH, and Ω_{arag} variations in the SAB are primarily controlled by atmospheric CO_2 increase, while carbonate chemistry in the MAB is modified significantly by salinity variations, which is driven by physical processes that bring in different water masses. The seasonal asymmetry in the evolution of long-term change leads to the change in the seasonal-cycle amplitudes of carbonate chemistry variables. Undersaturation will occur first in the MAB where both the seasonal amplitude and the change in the seasonal amplitude of Ω_{arag}

over time are larger than those of the SAB and the open ocean. The neural-network algorithms for estimating the carbonate chemistry variables in the MAB and the SAB can be used in other coastal regions where enough $f\text{CO}_2$ data exist to train a neural network and it could be added to global ocean models to better capture the changes of carbonate chemistry variables in coastal regions.

Acknowledgments

Seawater $f\text{CO}_2$ data were obtained from SOCAT version 6 data server (<https://www.socat.info/index.php/version-6/>). CarbonTracker CO_2 data were obtained from NOAA's Earth System Research Laboratory (ESRL) Global Monitoring Division through FTP access to netCDF files (<ftp://afnp.cmdl.noaa.gov/products/carbontracker/co2/molefractions/>). Mauna Loa CO_2 data were obtained from NOAA's ESRL Global Monitoring Division through its data server at <https://www.esrl.noaa.gov/gmd/ccgg/trends/data.html>. OISST version 2 data were obtained from NOAA's ESRL Physical Science Division through its data server at <https://www.esrl.noaa.gov/psd/data/gridded/data.noaa.oisst.v2.html>. EN4 temperature and salinity data were obtained from Met Office Hadley Center through its data server at <https://www.metoffice.gov.uk/hadobs/en4/download-en4-2-1.html>. The interpolated monthly gridded data sets presented in this work are available at <https://www.nodc.noaa.gov/ocads/data/0208346.xml>. Financial support for this work was provided by NOAA's Ocean Acidification Program.

This research was carried out, in part, under the auspices of the Cooperative Institute for Marine and Atmospheric Studies (CIMAS), a Cooperative Institute of the University of Miami and the National Oceanic and Atmospheric Administration (cooperative agreement #NA15OAR4320064).

References

- Aires, F., Prigent, C., & Rossow, W. B. (2004). Neural network uncertainty assessment using Bayesian statistics with application to remote sensing: 3. Network Jacobians. *Journal of Geophysical Research*, 109, D10305. <https://doi.org/10.1029/2003JD004175>
- Atkinson, L. P., Lee, T. N., Blanton, J. O., & Chandler, W. S. (1983). Climatology of the southeastern United States continental shelf waters. *Journal of Geophysical Research*, 88(Nc8), 4705–4718.
- Bailey, W. B., & Hachey, H. B. (1951). The vertical temperature structure of the Labrador current. *Proceedings of the Nova Scotia Institute of science*, 22(4), 34–40.
- Bakker, D. C. E., Pfeil, B., Landa, C. S., Metzl, N., O'Brien, K. M., Olsen, A., et al. (2016). A multi-decade record of high-quality $f\text{CO}_2$ data in version 3 of the Surface Ocean CO_2 Atlas (SOCAT). *Earth System Science Data*, 8(2), 383–413. <https://doi.org/10.5194/essd-8-383-2016>
- Bates, N. R., Michaels, A. F., & Knap, A. H. (1996). Seasonal and interannual variability of oceanic carbon dioxide species at the U.S. JGOFS Bermuda Atlantic time-series study (BATS) site. *Deep Sea Research, Part II*, 43(2–3), 347–383. [https://doi.org/10.1016/0967-0645\(95\)00093-3](https://doi.org/10.1016/0967-0645(95)00093-3)
- Bittig, H. C., Steinhoff, T., Claustre, H., Fiedler, B., Williams, N. L., Sauzède, R., et al. (2018). An alternative to static climatologies: Robust estimation of open ocean CO_2 variables and nutrient concentrations from T, S, and O_2 data using Bayesian neural networks. *Frontiers in Marine Science*, 5. <https://doi.org/10.3389/fmars.2018.00328>
- Cai, W., Xu, Y., Feely, R. A., et al. (2020). Controls on surface water carbonate chemistry along North American ocean margins. *Nature Communications*, 11(1), 2691. <https://doi.org/10.1038/s41467-020-16530-z>
- Cai, W. J., Hu, X., Huang, W. J., Jiang, L. Q., Wang, Y., Peng, T. H., & Zhang, X. (2010). Alkalinity distribution in the western north Atlantic Ocean margins. *Journal of Geophysical Research*, 115, C08014. <https://doi.org/10.1029/2009JC005482>
- Cai, W.-J., Hu, X., Huang, W. J., Murrell, M. C., Lehrter, J. C., Lohrenz, S. E., et al. (2011). Acidification of subsurface coastal waters enhanced by eutrophication. *Nature Geoscience*, 4(11), 766–770. <https://doi.org/10.1038/ngeo1297>
- Carter, B. R., Feely, R. A., Williams, N. L., Dickson, A. G., Fong, M. B., & Takeshita, Y. (2018). Updated methods for global locally interpolated estimation of alkalinity, pH, and nitrate. *Limnology and Oceanography: Methods*, 16(2), 119–131. <https://doi.org/10.1002/lom3.10232>
- Chapman, D. C., & Beardsley, R. C. (1989). On the origin of shelf water in the Middle Atlantic Bight. *Journal of Physical Oceanography*, 19(3), 384–391. [https://doi.org/10.1175/1520-0485\(1989\)019<0384:OTOOSW>2.0.CO;2](https://doi.org/10.1175/1520-0485(1989)019<0384:OTOOSW>2.0.CO;2)
- Chen, S., Hu, C., Barnes, B. B., Wanninkhof, R., Cai, W. J., Barbero, L., & Pierrot, D. (2019). A machine learning approach to estimate surface ocean $p\text{CO}_2$ from satellite measurements. *Remote Sensing of Environment*, 228, 203–226. <https://doi.org/10.1016/j.rse.2019.04.019>
- Clonley, M. C. et al. (2015). The South Atlantic Bight marine assessment: Species, habitats and ecosystems. The Nature Conservancy, Eastern U.S. Division. <http://nature.ly/marineSAtlanticBightERA>
- Czaja, A., & Frankignoul, C. (2002). Observed impact of Atlantic SST anomalies on the North Atlantic oscillation. *Journal of Climate*, 15(6), 606–623. [https://doi.org/10.1175/1520-0442\(2002\)015<0606:OIOASA>2.0.CO;2](https://doi.org/10.1175/1520-0442(2002)015<0606:OIOASA>2.0.CO;2)
- DeGrandpre, M. D., Olbu, G. J., Beatty, C. M., & Hammar, T. R. (2002). Air-sea CO_2 fluxes on the US Middle Atlantic Bight. *Deep-Sea Research Part II-Topical Studies in Oceanography*, 49(20), 4355–4367. [https://doi.org/10.1016/S0967-0645\(02\)00122-4](https://doi.org/10.1016/S0967-0645(02)00122-4)
- Doney, S. C., Fabry, V. J., Feely, R. A., & Kleypas, J. A. (2009). Ocean acidification: The other CO_2 problem. *Annual Review of Marine Science*, 1(1), 169–192. <https://doi.org/10.1146/annurev.marine.010908.163834>
- Fassbender, A. J., Rodgers, K. B., Palevsky, H. I., & Sabine, C. L. (2018). Seasonal asymmetry in the evolution of surface ocean $p\text{CO}_2$ and pH thermodynamic drivers and the influence on sea-air CO_2 flux. *Global Biogeochemical Cycles*, 32, 1476–1497. <https://doi.org/10.1029/2017GB005855>
- Feely, R. A., Sabine, C. L., Hernandez-Ayon, J. M., Ianson, D., & Hales, B. (2008). Evidence for upwelling of corrosive "acidified" water onto the continental shelf. *Science*, 320(5882), 1490–1492. <https://doi.org/10.1126/science.1155676>
- Goldsmith, K. A., et al. (2019). Scientific considerations for acidification monitoring in the U.S. mid-Atlantic region. *Estuarine, Coastal and Shelf Science*, 225, 106189. <https://doi.org/10.1016/j.ecss.2019.04.023>
- Good, S. A., Martin, M. J., & Rayner, N. A. (2013). EN4: Quality controlled ocean temperature and salinity profiles and monthly objective analyses with uncertainty estimates. *Journal of Geophysical Research: Oceans*, 118, 6704–6716. <https://doi.org/10.1002/2013jc009067>
- Grodsky, S. A., Reul, N., Chapron, B., Carton, J. A., & Bryan, F. O. (2017). Interannual surface salinity on northwest Atlantic shelf. *Journal of Geophysical Research: Oceans*, 122, 3638–3659. <https://doi.org/10.1002/2016jc012580>
- Gruber, N., Keeling, C. D., & Bates, N. R. (2002). Interannual variability in the North Atlantic Ocean carbon sink. *Science*, 298(5602), 2374–2378. <https://doi.org/10.1126/science.1077077>
- Hagan, M. T., & Menhaj, M. (1994). Training feedforward networks with the Marquardt algorithm. *IEEE Transactions on Neural Networks*, 5(6), 989–993. <https://doi.org/10.1109/72.329697>
- Harris, K. E., DeGrandpre, M. D., & Hales, B. (2013). Aragonite saturation state dynamics in a coastal upwelling zone. *Geophysical Research Letters*, 40, 2720–2725. <https://doi.org/10.1002/grl.50460>
- Hofmann, G. E., Smith, J. E., Johnson, K. S., Send, U., Levin, L. A., Micheli, F., et al. (2011). High-frequency dynamics of ocean pH: A multi-ecosystem comparison. *PLoS ONE*, 6(12), e28983. <https://doi.org/10.1371/journal.pone.0028983>
- Jiang, L.-Q., Cai, W.-J., Wanninkhof, R., Wang, Y., & Lüger, H. (2008). Air-sea CO_2 fluxes on the U.S. South Atlantic Bight: Spatial and seasonal variability. *Journal of Geophysical Research: Oceans*, 113, C07019. <https://doi.org/10.1029/2007JC004366>
- Kwiatkowski, L., & Orr, J. C. (2018). Diverging seasonal extremes for ocean acidification during the twenty-first century. *Nature Climate Change*, 8(2), 141–145. <https://doi.org/10.1038/s41558-017-0054-0>
- Landschützer, P., N. Gruber and D. C. E. Bakker (2017). An updated observation-based global monthly gridded sea surface $p\text{CO}_2$ and air-sea CO_2 flux product from 1982 through 2015 and its monthly climatology (NCEI accession 0160558). Version 2.2. NOAA National Centers for Environmental Information. Dataset. [2017-07-11]

- Landschützer, P., Gruber, N., Bakker, D. C. E., Stemmler, I., & Six, K. D. (2018). Strengthening seasonal marine CO₂ variations due to increasing atmospheric CO₂. *Nature Climate Change*, 8(2), 146–150. <https://doi.org/10.1038/s41558-017-0057-x>
- Laruelle, G. G., Cai, W. J., Hu, X., Gruber, N., Mackenzie, F. T., & Regnier, P. (2018). Continental shelves as a variable but increasing global sink for atmospheric carbon dioxide. *Nature Communications*, 9(1), 454. <https://doi.org/10.1038/s41467-017-02738-z>
- Lee, T. N., Yoder, J. A., & Atkinson, L. P. (1991). Gulf stream frontal eddy influence on productivity of the Southeast United States continental shelf. *Journal of Geophysical Research*, 96(C12), 22,191–22,205. <https://doi.org/10.1029/91JC02450>
- Lueker, T. J., Dickson, A. G., & Keeling, C. D. (2000). Ocean pCO₂ calculated from dissolved inorganic carbon, alkalinity, and equations for K₁ and K₂: Validation based on laboratory measurements of CO₂ in gas and seawater at equilibrium. *Marine Chemistry*, 70(1–3), 105–119. [https://doi.org/10.1016/S0304-4203\(00\)00022-0](https://doi.org/10.1016/S0304-4203(00)00022-0)
- MacKay, D. J. C. (1995). Probable networks and plausible predictions—A review of practical Bayesian methods for supervised neural networks. *Network: Computation in Neural Systems*, 6(3), 469–505. https://doi.org/10.1088/0954-898X_6_3_011
- Neal, R. M. (1996). *Bayesian learning for neural networks*. Springer, New York, NY: Springer-Verlag New York, Inc. <https://doi.org/10.1007/978-1-4612-0745-0>
- Orr, J. C., Epitalon, J. M., Dickson, A. G., & Gattuso, J. P. (2018). Routine uncertainty propagation for the marine carbon dioxide system. *Marine Chemistry*, 207, 84–107. <https://doi.org/10.1016/j.marchem.2018.10.006>
- Orr, J. C., Epitalon, J. M., & Gattuso, J. P. (2015). Comparison of ten packages that compute ocean carbonate chemistry. *Biogeosciences*, 12(5), 1483–1510. <https://doi.org/10.5194/bg-12-1483-2015>
- Orr, J. C., Fabry, V. J., Aumont, O., Bopp, L., Doney, S. C., Feely, R. A., et al. (2005). Anthropogenic ocean acidification over the twenty-first century and its impact on calcifying organisms. *Nature*, 437(7059), 681–686. <https://doi.org/10.1038/nature04095>
- Percival, D. B., & Walden, A. T. (1993). *Spectral analysis for physical applications: Multitaper and conventional univariate techniques*. Cambridge: Cambridge University Press. <https://doi.org/10.1017/CBO9780511622762>
- Peters, W., Jacobson, A. R., Sweeney, C., Andrews, A. E., Conway, T. J., Masarie, K., et al. (2007). An atmospheric perspective on North American carbon dioxide exchange: CarbonTracker. *Proceedings of the National Academy of Sciences of the United States of America*, 104(48), 18925–18930. <https://doi.org/10.1073/pnas.0708986104>
- Reynolds, R. W., Rayner, N. A., Smith, T. M., Stokes, D. C., & Wang, W. Q. (2002). An improved in situ and satellite SST analysis for climate. *Journal of Climate*, 15(13), 1609–1625. [https://doi.org/10.1175/1520-0442\(2002\)015<1609:AIISAS>2.0.CO;2](https://doi.org/10.1175/1520-0442(2002)015<1609:AIISAS>2.0.CO;2)
- Reynolds, R. W., Smith, T. M., Liu, C., Chelton, D. B., Casey, K. S., & Schlax, M. G. (2007). Daily high-resolution-blended analyses for sea surface temperature. *Journal of Climate*, 20(22), 5473–5496. <https://doi.org/10.1175/2007JCLI1824.1>
- Saba, G. K., Wright-Fairbanks, E., Chen, B., Cai, W. J., Barnard, A. H., Jones, C. P., et al. (2019). The development and validation of a profiling glider deep ISFET-based pH sensor for high resolution observations of coastal and ocean acidification. *Frontiers in Marine Science*, 6, 664. <https://doi.org/10.3389/fmars.2019.00664>
- Salisbury, J. E., & Jönsson, B. F. (2018). Rapid warming and salinity changes in the Gulf of Maine alter surface ocean carbonate parameters and hide ocean acidification. *Biogeochemistry*, 141, 401–418. <https://doi.org/10.1007/210533-018-0505-3>
- Sasse, T. P., McNeil, B. I., Matear, R. J., & Lenton, A. (2015). Quantifying the influence of CO₂ seasonality on future aragonite undersaturation onset. *Biogeosciences*, 12(20), 6017–6031. <https://doi.org/10.5194/bg-12-6017-2015>
- Signorini, S. R., Mannino, A., Najjar, R. G. Jr., Friedrichs, M. A. M., Cai, W. J., Salisbury, J., et al. (2013). Surface ocean pCO₂ seasonality and sea-air CO₂ flux estimates for the north American east coast. *Journal of Geophysical Research: Oceans*, 118, 5439–5460. <https://doi.org/10.1002/jgrc.20369>
- Strong, A. L., Kroeker, K. J., Teneva, L. T., Mease, L. A., & Kelly, R. P. (2014). Ocean acidification 2.0: Managing our changing coastal ocean chemistry. *Bioscience*, 64(7), 581–592. <https://doi.org/10.1093/biosci/biu072>
- Takahashi, T., Sutherland, S. C., Feely, R. A., & Wanninkhof, R. (2006). Decadal change of the surface water pCO₂ in the North Pacific: A synthesis of 35 years of observations. *Journal of Geophysical Research*, 111, C07S05. <https://doi.org/10.1029/2005JC003074>
- Thomas, A. C., et al. (2017). Seasonal trends and phenology shifts in sea surface temperature on the North American northeastern continental shelf. *Elementa-Science of the Anthropocene*, 5.
- Thomson, D. J. (1982). Spectrum estimation and harmonic analysis. *Proceedings of the IEEE*, 70(9), 1055–1096. <https://doi.org/10.1109/PROC.1982.12433>
- Turk, D., Wang, H., Hu, X., Gledhill, D. K., Wang, Z. A., Jiang, L., & Cai, W.-J. (2019). Time of emergence of surface ocean carbon dioxide trends in the North American coastal margins in support of ocean acidification observing system design. *Frontiers in Marine Science*, <https://doi.org/10.3389/fmars.2019.00091>
- Uppström, L. R. (1974). The boron/chlorinity ratio of deep-sea water from the Pacific Ocean. *Deep Sea Research and Oceanographic Abstracts*, 21(2), 161–162. [https://doi.org/10.1016/0011-7471\(74\)90074-6](https://doi.org/10.1016/0011-7471(74)90074-6)
- Van Heuven, S., Pierrot, D., Rae, J. W. B., & Wallace, D. W. R. (2009). *MATLAB program developed for CO₂ system calculations, carbon dioxide information analysis center, Oak Ridge National Laboratory*. Oak Ridge, Tennessee: U.S. Department of Energy.
- Vargas, C. A., Contreras, P. Y., Pérez, C. A., Sobarzo, M., Saldías, G. S., & Salisbury, J. (2016). Influences of riverine and upwelling waters on the coastal carbonate system off Central Chile and their ocean acidification implications. *Journal of Geophysical Research: Biogeosciences*, 121, 1468–1483. <https://doi.org/10.1002/2015JG003213>
- Velasco, R., Cheynet, P., Muller, J. D., Ecoffet, R., & Buchner, S. (1997). Artificial neural network robustness for on-board satellite image processing: Results of upset simulations and ground tests. *IEEE Transactions on Nuclear Science*, 44(6), 2337–2344. <https://doi.org/10.1109/23.659057>
- Visbeck, M. H., Hurrell, J. W., Polvani, L., & Cullen, H. M. (2001). The North Atlantic oscillation: Past, present, and future. *Proceedings of the National Academy of Sciences of the United States of America*, 98(23), 12876–12877. <https://doi.org/10.1073/pnas.231391598>
- Wallace, R. B., Baumann, H., Grear, J. S., Aller, R. C., & Gobler, C. J. (2014). Coastal Ocean acidification: The other eutrophication problem. *Estuarine, Coastal and Shelf Science*, 148, 1–13. <https://doi.org/10.1016/j.ecss.2014.05.027>
- Weiss, R. F. (1974). Carbon dioxide in water and seawater: The solubility of a non-ideal gas. *Marine Chemistry*, 2(3), 203–215. [https://doi.org/10.1016/0304-4203\(74\)90015-2](https://doi.org/10.1016/0304-4203(74)90015-2)
- Weiss, R. F., & Price, B. A. (1980). Nitrous oxide solubility in water and seawater. *Marine Chemistry*, 8(4), 347–359. [https://doi.org/10.1016/0304-4203\(80\)90024-9](https://doi.org/10.1016/0304-4203(80)90024-9)